Modelling time-lapse shear-wave velocity changes in an unsaturated soil embankment due to water infiltration and drainage

Suzaki, Atsushi; Minato, Shohei; Ghose, Ranajit; Konishi, Chisato; Sakai, Naoki

Publication date
2017

Published in
First Break

Citation (APA)
Suzaki, A., Minato, S., Ghose, R., Konishi, C., & Sakai, N. (2017). Modelling time-lapse shear-wave velocity changes in an unsaturated soil embankment due to water infiltration and drainage. *First Break*, *35*(8), 81-90.

This is a postprint of an article published in: First Break
Issue: Vol 35, No 8, August 2017 pp. 81 - 90
http://www.earthdoc.org/publication/publicationdetails/?publication=89811

Modelling time-lapse shear-wave velocity changes in an unsaturated soil embankment due to water infiltration and drainage

Authors: Atsushi Suzaki [1,2*], Shohei Minato[2], Ranajit Ghose[2], Chisato Konishi[1], Naoki Sakai[3]

1: OYO Corporation, Japan

2: Section of Applied Geophysics and Petrophysics, Department of Geoscience and Engineering, Delft University of Technology, The Netherlands.

3: National Research Institute for Earth Science and Disaster Prevention (NIED), Japan

*: Corresponding author: a.suzaki@tudelft.nl

Abstract

Soil suction and degree of saturation play an important role in controlling the hydraulic and mechanical properties of the unsaturated soil in the vadose zone. Due to the sensitivity to inter-particle stress, the velocity of shear wave (V_S) is expected to sense the suction changes during fluid transportation in an unsaturated soil. In this study, we investigate the significance of unsaturated soil properties in temporal and spatial V_S changes, considering water infiltration and drainage in an unsaturated embankment subjected to rainfall. We numerically model V_S changes, simultaneously considering fluid flow in unsaturated soil and the small-strain shear modulus as a function of suction and confining stress, and using soil-water characteristics curve. The results show that the V_S changes are controlled more by suction changes than by density changes. The comparison of the numerical prediction with the results of a field-scale experiment at an artificial embankment presents clear indications of water infiltration and drainage. Monitoring V_S changes in unsaturated soils can potentially be used to estimate fluid distribution and in-situ, dynamic fluid transportation in the vadose zone. This will find many important applications, e.g., pollution analyses at waste disposal sites, assessment of desertification, water resources and agricultural sustainability, and estimation of the stability of geoengineering structures, soil embankments and natural slopes.

1. Introduction

The partially saturated vadose zone, located between the Earth's surface and the water table, is made of soil particles, water and air. The water in the vadose zone can be transient percolating water which moves downward to join the phreatic water below the water table or the capillary water held above the water table by surface tension (internal pore pressure less than the atmospheric pressure). The distribution and transport of fluids in the vadose zone have a significant influence on the human life and the environment. For example, the dynamic transportation of fluids in the vadose zone is an important factor which controls the pollution at a near-surface, hazardous waste site (Mercer and Cohen, 1990), affects the desertification in arid/semiarid areas (Scanlon et al., 2003), and determines the sensitivity of water resources to the climate change (Green et al., 2011). The distribution of water in the vadose zone also affects the microbial processes, e.g., biodegradation, which is necessary in assessing agricultural sustainability (Holden and Fierer, 2005). Last but not the least, the dynamic fluid transportation in the vadose zone causes dynamic changes in the yield strength of the unsaturated soil. Therefore, it is critically important in estimating the stability of earth retaining structures (e.g., river dykes and embankment dams) and natural slopes (e.g., Collins and Znidarcic, 2004).

Soil suction (a function of capillary pressure) and the degree of saturation (a function of water content) play an important role in controlling the hydraulic and mechanical properties of unsaturated soil in the vadose zone. Depending on the degree of saturation (S_r), unsaturated soils shows different values of suction (s). The s-S_r curve, known as the soil-water characteristics curve (SWCC), is the most important piece of information that characterizes the unsaturated soils. Figure 1 shows a typical plot of SWCC. While the suction is zero at the fully saturated condition, it increases as the degree of saturation decreases. Depending on soil texture, SWCC shows different trends. At the same degree of saturation, clayey soils show larger suction values than sandy soils (Figure 1). This is because clayey soils represent smaller pore sizes (capillary radii) than sandy soils, thus creating a larger capillary pressure (Fredlund et al., 2012).

Hydraulic permeability in unsaturated soils depends on suction (Leong and Rahardjo, 1997). SWCC plays a major role in determining the hydraulic permeability because it is related to the pore-size distributions (Fredlund and Xing, 1994). Furthermore, suction being an inter-particle force acting on the soil skeleton, the mechanical properties of the unsaturated soil, e.g., shear strength and elastic moduli are also controlled by this force (Han and Vanapalli, 2016).

In near-surface geophysics, shear-wave velocity (V_S) is an important target in field measurements. This is because V_s directly relates to the in-situ value of the small-strain rigidity of soil, which is important in all dynamic loading problems in geotechnical engineering. V_s is sensitive to the state of the grain-to-grain contact. The sensitivity of V_S can be utilized to monitor the in-situ stress in soil (Ghose, 2012). Also, Vs is expected to measure the changes in the inter-particle forces (e.g., suction changes) during fluid movement in the vadose zone. "Bergamo et al. (2016) report a long-term experiment in which VS at a railway embankment is monitored. The result shows that measuring VS can be a promising approach to estimate non-invasively the temporal and spatial changes in the water content in soil."Pasquet et al. (2016) perform physical-model experiments using glass beads, where they evaluate the sensitivity of compressional (P) wave traveltimes and surface-wave dispersion curves (linking changes in V_s) to changes in water level and the thickness of the capillary fringe. On a practical front, due to a considerably smaller value of the velocity of shear wave compared to that of P wave in soft, unconsolidated soils, shear wave generally offers significantly shorter wavelength than P wave, and hence much higher spatial resolution, for the similar frequencies. This fact, together with the sensitivity of shear-wave to subtle changes in the soil type, stress and the state of compaction, are attributed to the observed fine-scale spatial correlation of Vs with the strength-indicators of soil (e.g., Ghose and Goiudswaard, 2004; Ghose, 2012). Furthermore, V_S can be estimated using cost-effective surface-wave measurements.

The problem of modelling V_S changes in unsaturated soils due to fluid transportation calls for an interdisciplinary research. Understanding correctly the spatial/temporal V_S changes requires an integral knowledge linking soil physics, fluid dynamics, geotechnical engineering, and geophysics. Although this problem has drawn renewed interest recently in the geophysical community due to the development of the seismoelectric method (Zyserman et al., 2017), there are few studies which investigate the spatial and temporal V_S changes using approaches from these different disciplines, together with field geophysical measurements.

In this study, we look into the role of unsaturated soil properties in temporal and spatial V_S changes, considering water infiltration and drainage in an unsaturated soil embankment subjected to rainfall. Seepage failure of such structures, e.g., river dykes, dams, and natural slopes, due to water infiltration (rising water level and/or heavy rainfall) has often been a major threat to human life and environment (e.g., Rahardjo et al., 2001; Rico et al., 2008). In order to discuss the feasibility of in-situ monitoring, the magnitude of V_S changes and the spatial/temporal distribution of V_S are considered. For this purpose, we use the accumulated knowledge in geotechnical engineering and geophysics to incorporate the realistic properties/features of the embankment, i.e., dimension of dyke, SWCC, and water infiltration/drainage due to rainfall. Furthermore, in order to model realistically the shear modulus as a function of suction, we use existing experimental datasets and the recent advancements in the effective stress framework in unsaturated soil mechanics (e.g., Han and Vanapalli, 2016). Because the history of rainfall plays an important role in determining the spatio-temporal distribution of water (infiltration and drainage processes), we also solve the fluid transportation problem (seepage analysis) in unsaturated soil (Lam et al., 1987). The calculated V_S changes are then discussed using data from a recent field-scale experiment conducted on an artificial soil embankment (Konishi et al., 2015).

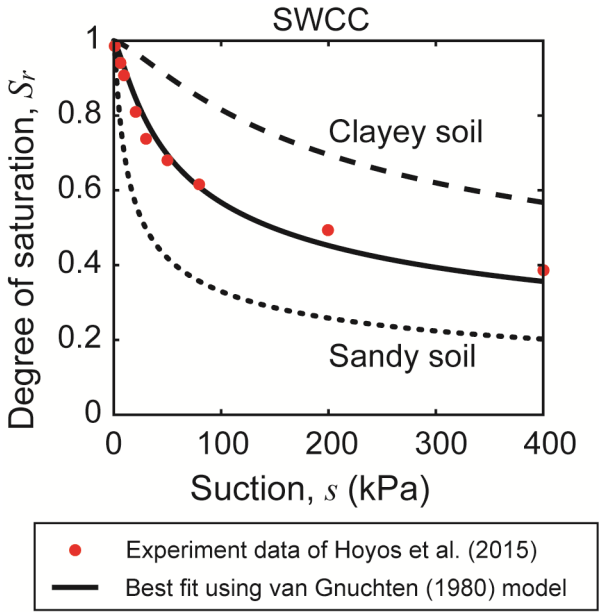

Figure 1: The soil-water characteristic curve (SWCC). Red dots show the experimental data for silty sand (Hoyos et al., 2015). Solid line is the best-fit curve using the model of van Genuchten (1980). Dotted and dashed lines represent curve for sandy soil and clayey soil, respectively.

2. Linking V_s to unsaturated soil properties: a role of SWCC

The distribution of water in unsaturated soil changes the inter-particle force (suction), which results in changes in V_S. Based on data from geotechnical laboratory experiments, where the small-strain shear modulus G_0 is estimated under controlled net confining stress (σ_c) and suction (s), V_S can be expressed in the following form (Sawangsuriya et al., 2009):

$$V_S(s,\sigma_c) = \sqrt{\frac{G_0(s,\sigma_c)}{\rho(S_r)}}. \quad (1)$$

The bulk density ρ is calculated as $\rho(S_r) = \phi S_r \rho_w + (1-\phi)\rho_g$, where ϕ is porosity, ρ_w is density of water, and ρ_g is density of grain.

The small-strain shear modulus of dry or saturated soils is generally expressed as:

$$G_0 = A(\sigma')^n, \quad (2)$$

where σ' is the mean effective stress and A is a coefficient representing material parameter associated with soil microstructure (fabric), void ratio and/or over-consolidation ratio (e.g., Hardin and Blandford, 1989). Contrary to the case of dry or saturated soils, a consistent model to represent G_0 in unsaturated soil does not exist yet (Sawangsuriya et a., 2009). In this study, we consider the following empirical model:

$$G_0(s,\sigma_C) = k_1(\sigma_C)^{k_2} + \Gamma \times S_r \times s, \quad (3)$$

where k_1, k_2 and Γ are fitting parameters. Han and Vanapalli (2016), among others, propose equation (3) and show that this equation is a fairly accurate representation for low suction (high saturation) values and for cohesionless soils with little-to-no clay content. Equation (3) presents G_0 as a sum of two terms: the first term represents the stress-dependence in the saturated condition where suction is zero, i.e., $A(\sigma_C)^n$, and the second term shows the effect of suction and degree of saturation. Therefore, the effect of SWCC (s-S_r relation) is evident in G_0 (equation (3)). Selection of this form of equation is inspired by the independent stress state variable approach for deriving shear strength of unsaturated soils (Fredlund et al., 1996; Sawangsuriya et al., 2009), where two chosen independent stress state variables are the net stress and the suction. Sawangsuriya et al. (2009) propose also an alternative model based on the Bishop-type effective stress σ' (Bishop, 1960):

$$\sigma' = \sigma_C + \chi \times s, \quad (4)$$

where χ is the Bishop's parameter which is considered to be related to the volume fraction of fluids occupying the pore space, or the degree of saturation (Nuth and Laloui, 2008), i.e., $\chi = \chi(S_r)$. Substituting this form for the effective stress to the general representation of G_0 shown in equation (2) gives

$$G_0(s,\sigma_C) = A(\sigma_C + S_r \times s)^n, \quad (5)$$

where we assume $\chi = S_r$. Sawangsuriya et al. (2009) point out using experimental data that G_0 predicted from these two models (equations (3) and (5)) show similar values in the low-suction range. Note that, considering the Bishop-type effective stress, Shen et al. (2016) propose a theoretical model to predict G_0 using the Hertz-Mindlin theory. The review of other various effective stress models in unsaturated soil is found in Nuth and Laloui (2008).

Once we obtain SWCC, equation (3) enables us to interpolate/extrapolate G_0 measured in the laboratory, leading to prediction of V_S values at various saturation conditions (equation (1)). We use the laboratory dataset for silty sand (Hoyos et al., 2015). The measured SWCC is first interpolated (Figure 1) by fitting the data using van Genuchten (1980) model, and then G_0 is obtained by surface-fitting using equation (3). Figure 2(a), 2(b) and 2(c) show the fitted G_0 surface (k_1 =2644, k_2 =0.568 and Γ=185). One can see that G_0 increases as the confining stress and/or the suction values increase. Equation (3) explains the observed data quite well.

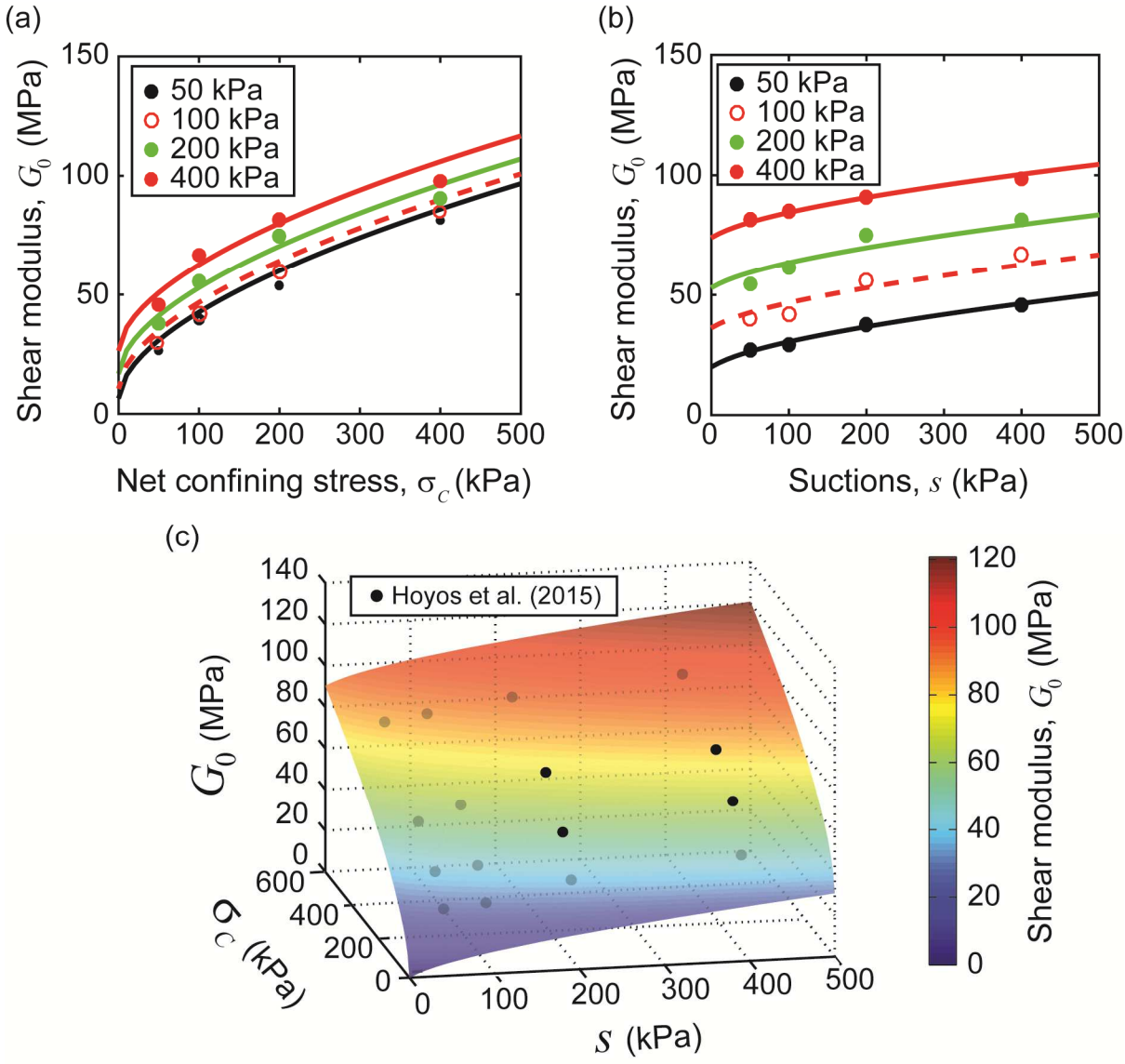

Figure 2: (a, b) The relationship between the small-strain shear modulus and the suction at different confining stress values: coloured dots/circles show the experimental data (Hoyos et al., 2015) and the continuous lines represent our best-fit estimates (equation 3). (c) The small-strain shear modulus interpolated using equation (3). This surface plot enables us to see G_0 as a continuous function of both variables (suction and confining stress), which is not possible from (a) or (b). Black dots show the experimental data (Hoyos et al., 2015).

3. Seepage analysis

In order to estimate the fluid flow in unsaturated soil, we consider a partially saturated porous medium where the flow obeys the Richards' equation (Richards, 1931; Lam et al., 1987). It is written in two dimensions as:

$$\frac{\partial}{\partial x}\left(K\frac{\partial h}{\partial x}\right)+\frac{\partial}{\partial y}\left(K\frac{\partial h}{\partial y}\right)=-\frac{\partial \theta}{\partial t}, \quad (6)$$

where K is the hydraulic conductivity or the coefficient of permeability (m/s), h the total head (m) which is the sum of pressure (suction) head and elevation head, and θ the volumetric water content. Unlike some earlier studies (e.g., Steenpass et al., 2010) focused on soil-surface temperature (at relatively shallower depth), we consider in this study only liquid water, as in common in geotechnical investigation. Note that the hydraulic conductivity K (m/s) is related to the permeability k (m^2) as $K = k\rho_f g/\mu$, where g is the acceleration due to gravity, ρ_f the density of the fluid, and μ the dynamic viscosity of the fluid. The hydraulic conductivity is a function of suction: $K(s) = K_{sat} \times K_r(s)$, where K_{sat} is the conductivity at the saturated condition; the relative conductivity $K_r(s)$ can be calculated from SWCC (van Genuchten, 1980). We solve equation (6) using the finite element method (FEM).

4. Water infiltration in an unsaturated embankment and V_S changes due to rainfall

Hydraulic properties of unsaturated soil depend on the suction. Therefore, when we consider water infiltration in an unsaturated embankment (river dykes, dams and natural slopes) due to rainfall, the history of rainfall (precipitation) plays an important role in determining the dynamic distribution of water content. In this section, we consider a realistic embankment model under a constant precipitation, in order to discuss the significance of suction and fluid flow in V_S changes in unsaturated embankments.

We consider a two dimensional problem using the embankment model shown in Figure 3(a). This model is inspired by the field-scale experiments of Konishi et al. (2015) where time-lapse V_S measurements, through surface wave dispersion monitoring, were performed on an artificial embankment under controlled rainfall. We assume that the embankment consists of silty sand characterized by SWCC and $G_{0,}$ as shown in Figure 1 and Figure 2, respectively. The hydraulic conductivity in saturated condition (K_{sat}) is assumed to be 8.3 $\times 10^{-5}$ m/s, which is in the typical range between clean sand and silty sand (Bear, 1972). The water table, which determines initial saturation/suction distribution under hydrostatic condition, is assumed to be at -2 m. Finally, the porosity (ϕ = 0.46) is known (measured) for this experiment, and the water density (ρ_w) and the grain density (ρ_g) are assumed to be 1000 kg/m^3 and 2600 kg/m^3, respectively. Here, we assume that the initial saturation distribution is controlled by the water table located at -2m, in order to discuss the primary effects of water infiltration from the surface due to rainfall. When we consider river dykes, however, the presence of river water at one side of the embankment also contributes to water infiltration and drainage processes, which can be modelled by seepage analysis using appropriate initial and boundary conditions. This is not attempted at present.

We perform the seepage analysis under a constant precipitation rate of 100 mm/h for 180 minutes (Figure 3(b)). The water drainage is then followed until t = 270 min. Figure 4 shows the spatial distribution of suction (Figure 4(a)), saturation (Figure 4(b)), and total head (Figure 4(c)) at each lapse time during water infiltration (t = 0, 70, 105 and 180 min) and water drainage (t = 210 and 270 min). Note that Figure 4 illustrates the results around the right-side slope of the embankment above the ground surface. However, we, in fact, calculate a larger area (80 m in width and 30 m in height) in order to minimize the boundary effects due to the finite dimension of the model. At t = 0 min, the suction, saturation and total head are in hydrostatic condition. Water infiltrates from the surface of the embankment, which decreases the suction and increases the saturation near the surface. The

unsaturated zone around the center of the embankment becomes narrow as time progresses (t = 0—180 min), because water flows towards the center of the embankment, which can also be distinguished by the flow vector (gradient of total head) shown in Figure 4(c). Once the rain stops at t = 180 min, the water in the embankment gets diffused, recovering with time toward the initial hydrostatic condition (water drainage stages, see t = 210 and 270 in Figure 4).

Next, we estimate the spatial and temporal changes in V_S from the calculated values of suction (s) and saturation (S_r), using equation (1) and (3). Here, we calculate the confining stress distribution (σ_c) from the vertical distribution of grain density. Figure 5 shows the calculated values of ρ, G_0, and V_S at three different spatial locations within the embankment, shown by small circles in Figure 3(a). The plots of temporal changes (Figure 5) show that the water infiltrates from the surface to a deeper level, and that ρ increases and G_0 decreases as the infiltration progresses (Figure 5(a) and 5(b)). The shallowest point (Y = 4.5 m) shows the largest changes in G_0 (Figure 5(b)). This is because the confining stress is small at this point and the relative effect of suction is large on G_0 (see equation 3). In the water drainage stage (after t = 180 min), V_S starts recovering towards the initial values. Finally, our calculation (Figure 5(c)) shows that the temporal changes in V_S are controlled more by the changes in G_0 than those in ρ, which indicates that the effect of suction dominates V_S changes.

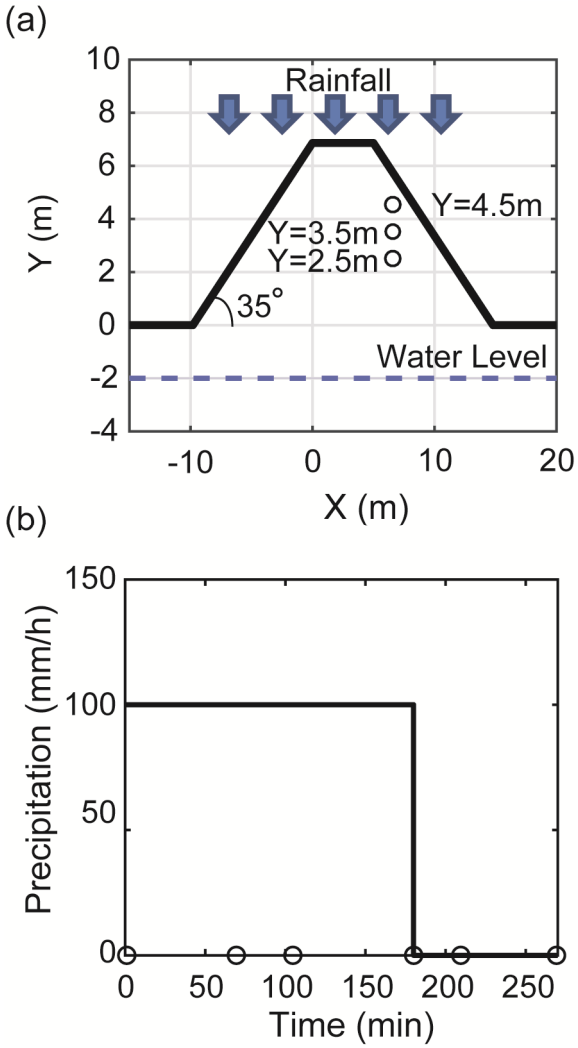

Figure 3: (a) Embankment model used in numerical modelling. Small open circles are the spatial locations where the temporal change of elastic properties are calculated and shown in Figure 5. (b) The time series of precipitation used in the numerical modelling. Open circles at the lower margin show times when the

spatial distribution of the unsaturated soil properties are investigated (Figure 4), corresponding to the field-scale experiments of Konishi et al. (2015).

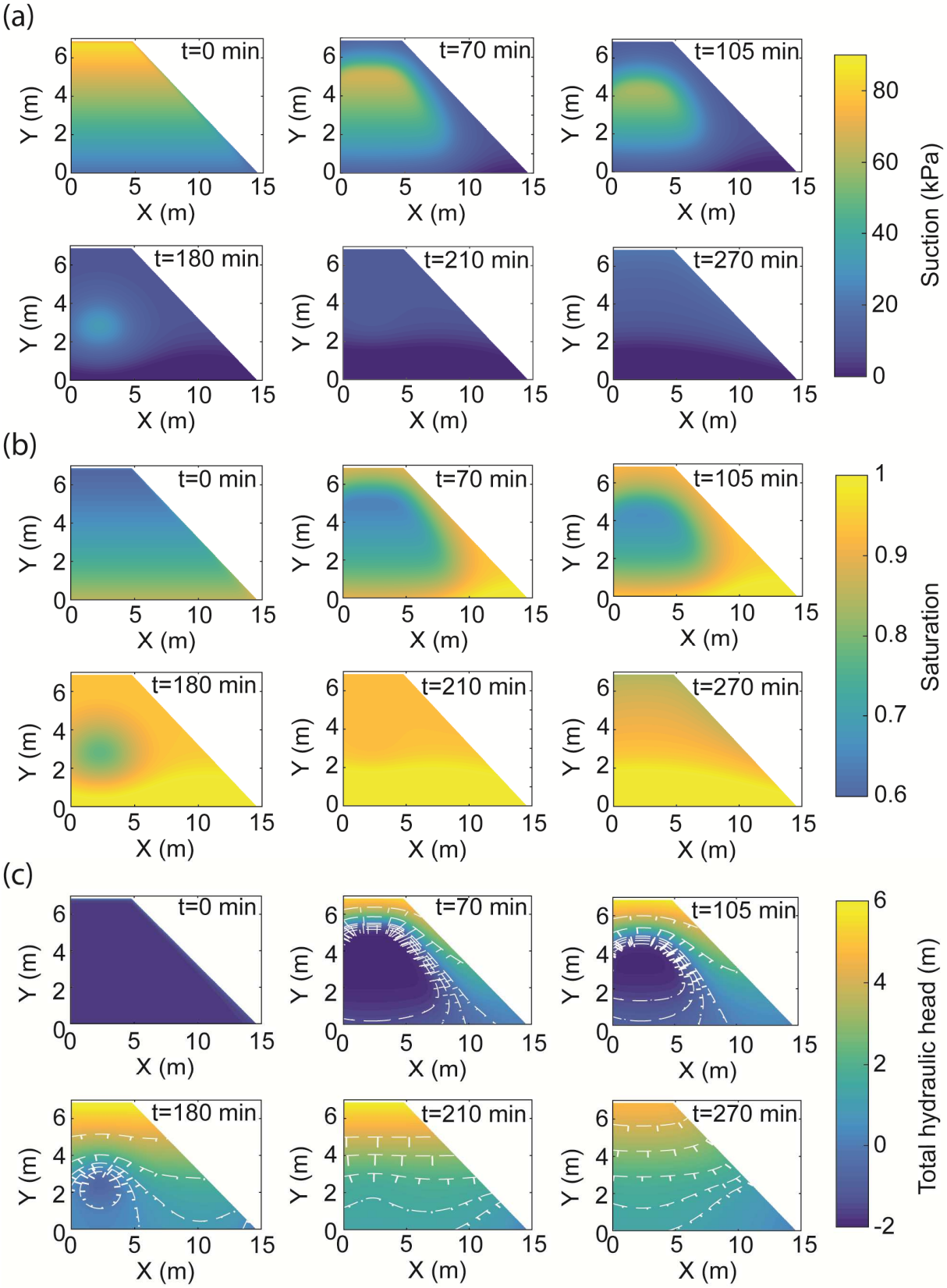

Figure 4 (a) Spatial distribution of the estimated suction at each lapse time. *t* = 0, 70, 105 and 180 min are in water infiltration stage, and *t* = 210 and 270 min are in water drainage stage (see open circles in Figure

3(b)). (b) Same as (a) but for the degree of saturation. (c) Same as (a) but for the total head. Contour lines and fluid flow vectors (gradient of the total head) are shown in (c).

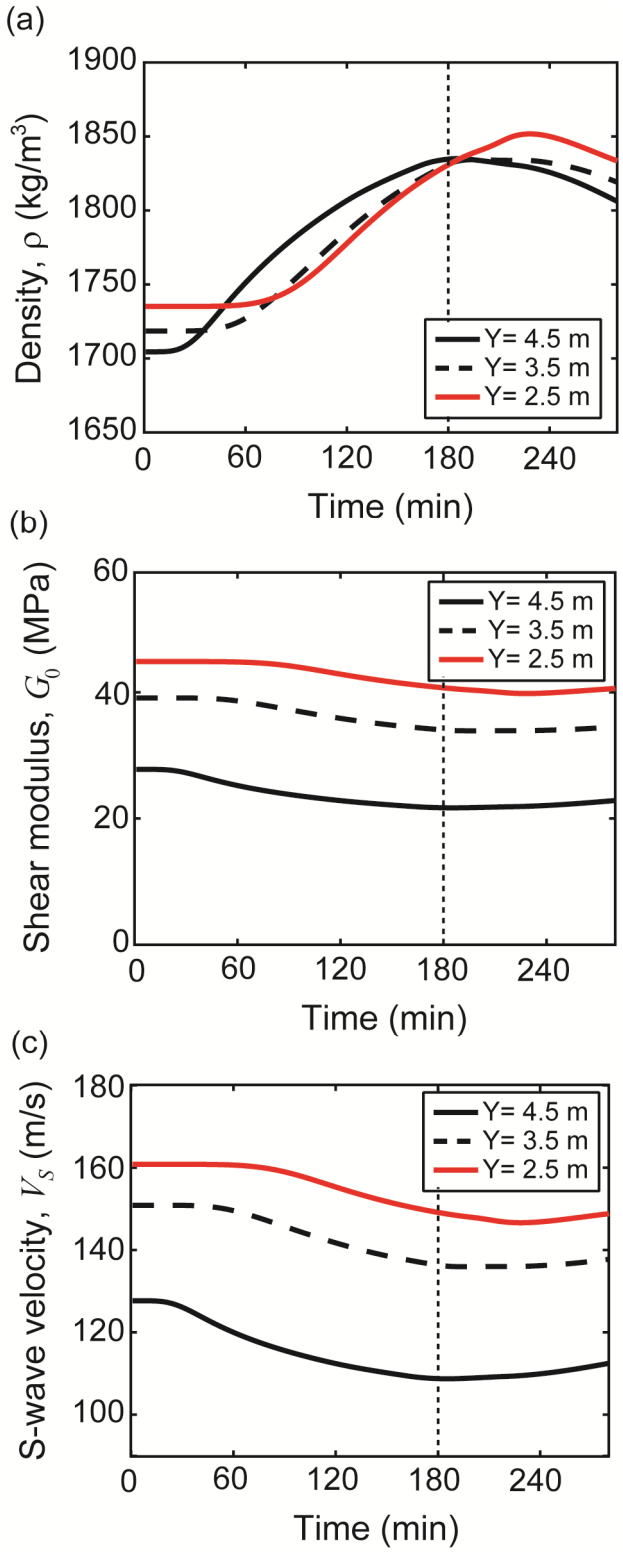

Figure 5: Temporal change of (a) ρ, (b) G_0 and (c) V_S at three locations shown in Figure 3(a). The vertical dashed line marks the time when the rain stops (t = 180).

5. V_S changes monitored in a field-scale experiment

Konishi et al. (2015) perform time-lapse V_S measurements at an artificial, field-scale embankment subjected to controlled rainfall. The dimensions of the soil embankment are almost identical to that shown in Figure 3(a). The test embankment mainly consists of sandy soil mixed with silt and clay (Takakura et al., 2012; Yoshioka et al., 2015). Konishi et al. (2015) use a rainfall simulator to realize a temporally varying precipitation (Figure 6(b)). They measure seismic surface waves (Rayleigh wave) in order to estimate the spatial distribution of V_S at the slope of the embankment. Figure 6(a) shows the fixed receiver array (24 geophones) positioned on the embankment slope. A vertical P-wave source (hammer impact) is used to generate the Rayleigh waves. The receivers are planted at 0.5 m interval along the slope. The source moves also by 0.5 m along the line. The time-lapse measurements comprise of an initial/base condition (t = 0 shown as "1st" in Figure 6(b)), the water infiltration stages (t = 70, 105 and 180 min, shown as "2nd","3rd" and "4th"), and the water drainage stages (t = 210 and 270 min, shown as "5th" and "6th").

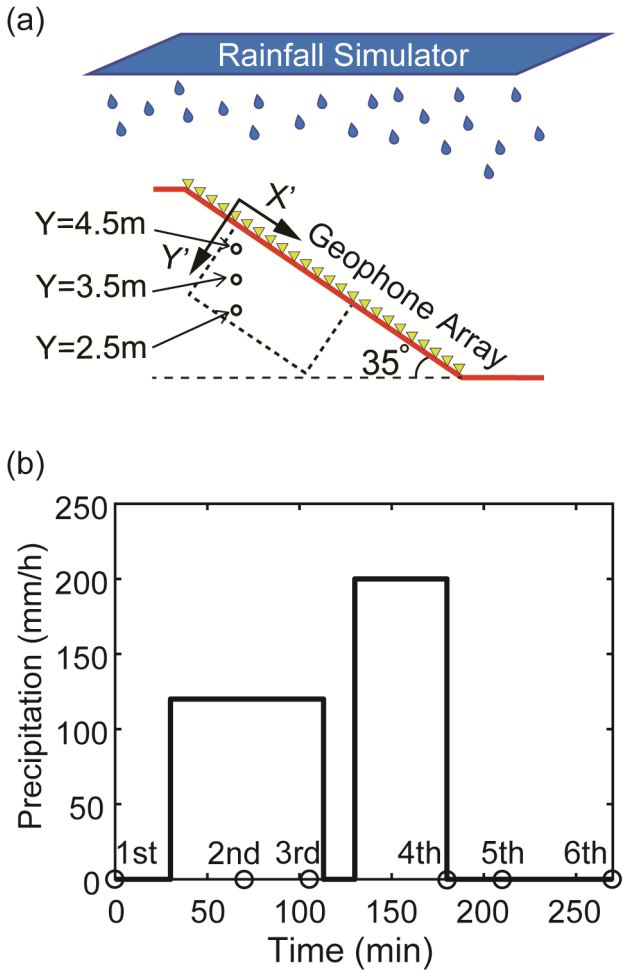

Figure 6: (a) Cross-section of the field-scale test embankment and the location of the fixed geophone array. Small open circle are the locations where the temporal changes are monitored (from time-lapse surface wave dispersion data) and shown in Figure 8(a). Dashed rectangle shows the spatial range of the V_s distribution shown in Figure 8(b). (b) The time series of rainfall in this field-scale measurement. Seismic surface wave measurements are made at the time shown by open circles in (b).

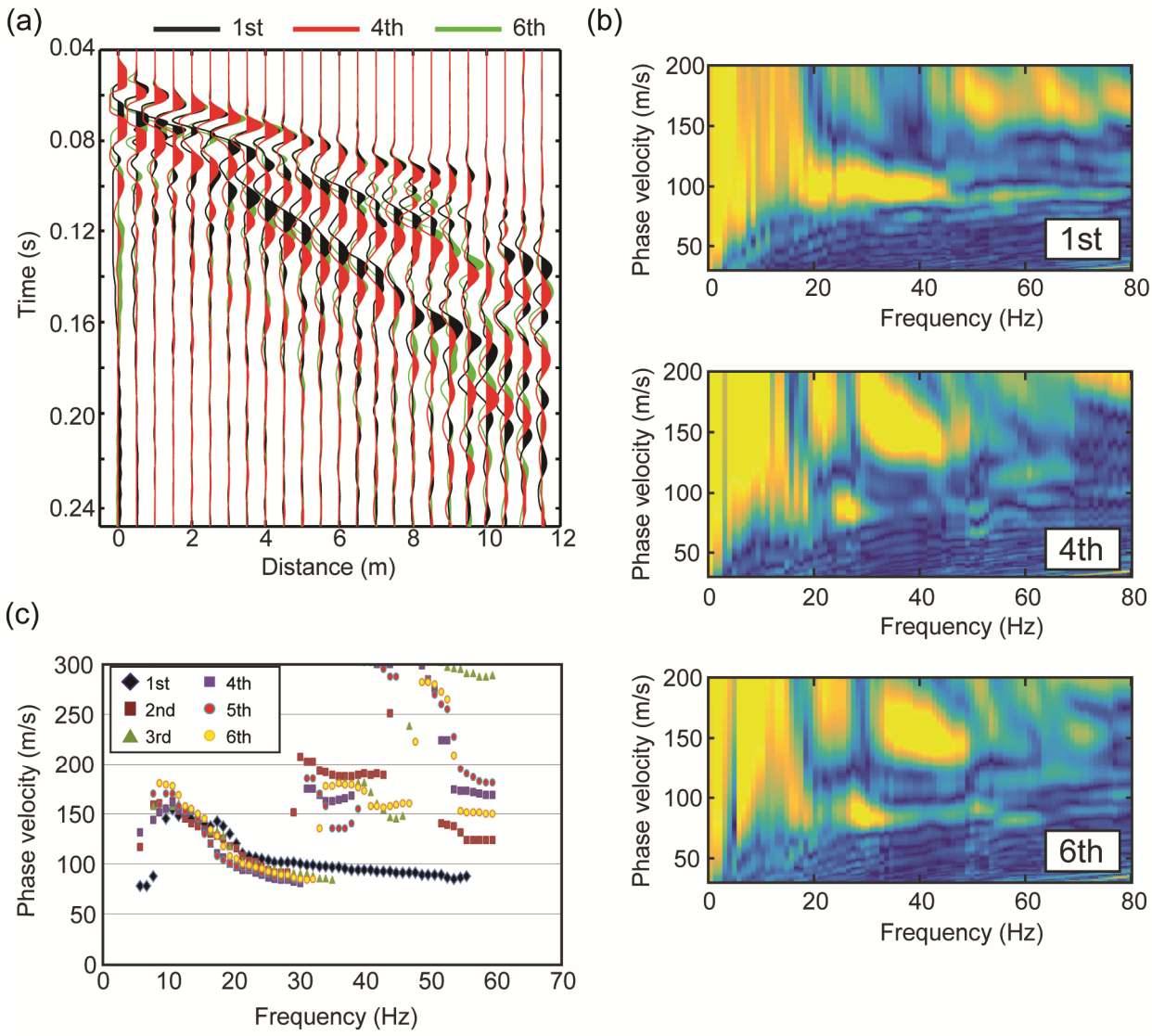

Figure 7: (a) Representative waveforms (shot gather) of 1st, 4th, and 6th measurements, when the source is located at the top of the embankment. (b) Dispersion images (MASW) using the data (shot gather) shown in (a). (c) Typical time-lapse dispersion curves picked for all 6 measurements, derived from a shot gather - in this case the source being located at the toe of the embankment (modified after Konishi et al., 2015).

Figure 7(a) shows an example of the observed surface (Rayleigh) waves due to the source located at the top of the embankment. We show three different waveforms: 1st measurement (black lines), 4th measurement (red lines), and 6th measurement (green lines). One can clearly see that the surface waves in the 4th measurement (red lines) arrive later than those in the 1st measurement (black lines), and those in the 6th measurement (green lines) arrive earlier than those in the 4th measurement (red lines). This indicates that at the 4th measurement (red lines), V_S decreases from the initial values due to water infiltration in the embankment (see Figure 6(b) after the rainfall, and that at the 6th measurement (green lines) V_S recovers towards the initial values due to water drainage from the embankment. This is confirmed also in the dispersion curves of the surface waves, which is estimated through multichannel analysis of surface waves (MASW , Park et al, 1999). Figure 7(b) shows the dispersion images of the waveforms in Figure 7(a) where the phase velocities of coherent surface waves are distinguished in yellow colour. The fundamental mode shows phase velocities ranging from 60 m/s to 180 m/s in the frequency range of 10--60 Hz. Although higher-order surface waves are present in the

4th and 6th measurements, the fundamental mode shows that the phase velocity at 10—60Hz decreases in the 4th measurement. Furthermore, the phase velocity in the 6th measurement increases from the 4th measurement, especially at the lower frequency range (10—30Hz). Figure 7(c) shows typical time-lapse dispersion curves (Konishi et al., 2015). The detected dispersion curves show that the phase velocity decreases in water infiltration stages (1st—4th measurements) and then slightly increases in water drainage stages (5-6th measurements) especially in 15—35 Hz range. These results suggest that the velocity starts recovering from the deeper part of the embankment.

In order to improve the lateral resolution of the V_S field, we next use a common-midpoint cross-correlation (CMPCC) analysis approach (Hayashi and Suzuki, 2004), where cross-correlation traces of surface waves measured using multiple source locations are sorted into CMP gathers. The estimated dispersion curves (fundamental mode) are then inverted to obtain an one-dimensional V_S structure at every CMP position, using a nonlinear least-squares inversion approach (Hayashi and Suzuki, 2004). Figure 8(a) shows the temporal V_S changes at three different spatial locations in the embankment, marked by circles in Figure 6(a). Similar to Figure 7, the estimated V_S decreases until t = 180 min, and then increases until the end of the measurements (t = 270 min). We also calculate the V_S reduction rate (R) from the initial values, which is defined as,

$$R(\%) = \frac{V_S(t=0) - V_S(t)}{V_S(t=0)} \times 100. \quad (7)$$

Figure 8(b) shows the spatial distribution of R. Note that Figure 8(b) is shown in the slope-oriented coordinate (see the dashed rectangle in Figure 6(a)) and $Y' = 0$ corresponds to the surface of the slope. The maximum magnitude of the estimated V_S reduction rate is 15% at $Y' = -1.5$ m at t = 180 min; also fine-scale alterations are observed at the shallow part of the slope. Here, however, we concentrate on the spatial boundary showing a sharp change in the V_S reduction rate (white dashed lines in Figure 8(b)), which represents the first-order effect of the water infiltration/drainage processes. The results show that the V_S reduction starts from the shallow part of the slope (t = 70 and 105 min), it progresses to a deeper level (t = 180 and 210 min), and then it recovers starting from the deeper part of the slope (t = 270 min).

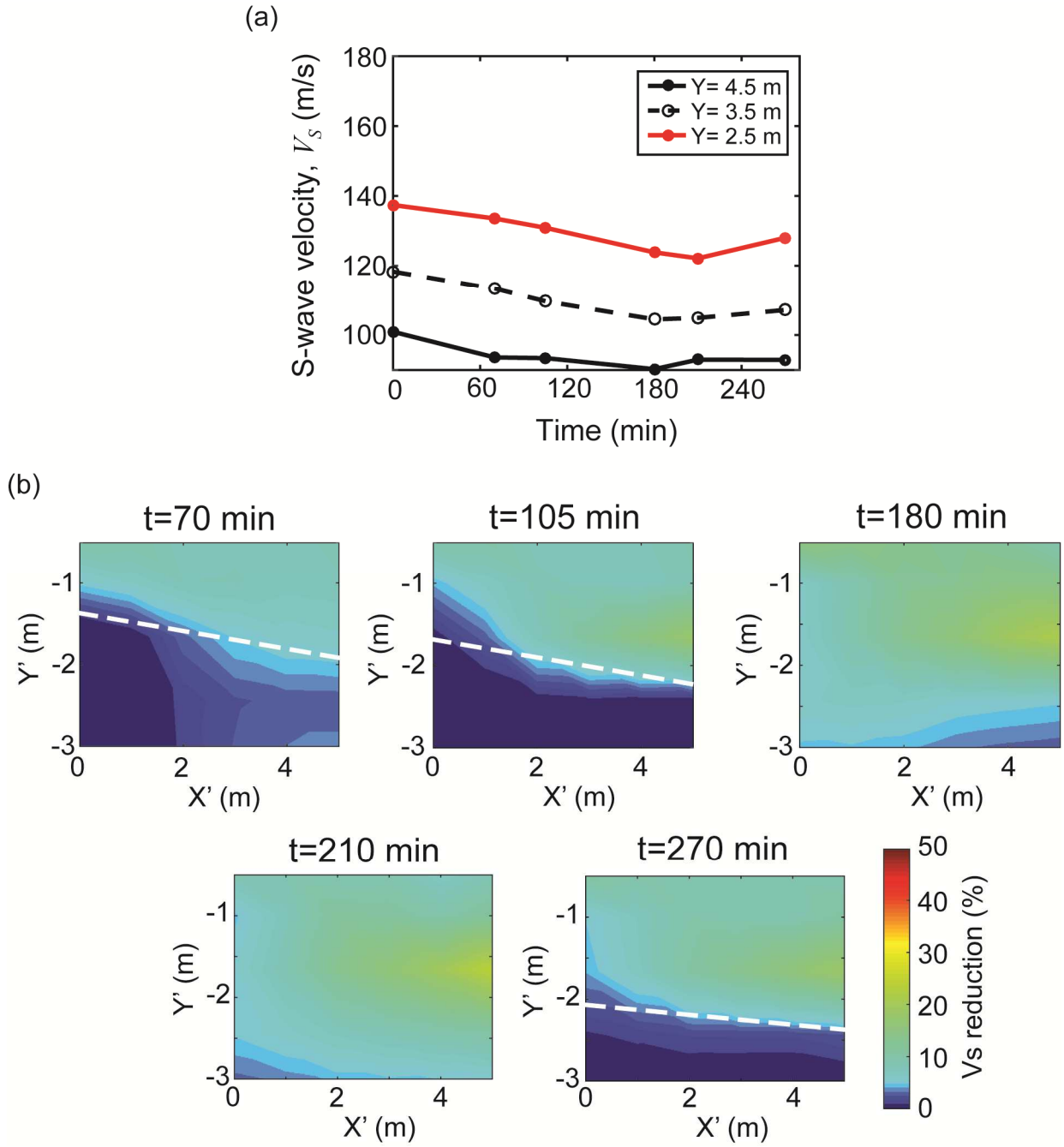

Figure 8: (a) Observed temporal changes of V_S in the field-scale experiment (modified after Konishi et al., 2015). Values at three spatial locations (small open circles in Figure 6(a)) are shown. (b) Spatial distribution of the V_S reduction rate R (equation 7) at each measurement (modified after Konishi et al., 2015). Positive values of R indicate a decrease of V_S from the initial values. White dashed lines mark the position of the boundary representing sharp changes in the V_S reduction rate, which is interpreted as to be indicating water infiltration and drainage.

Next, we perform the numerical modelling to estimate the V_S changes considering the same temporally varying precipitation as that shown in Figure 6(b). We use also the same embankment model as in the previous section. The obtained temporal changes of V_S at the three different locations (Figure 9(a)) and the spatial distribution of V_S reduction rate (Figure 9(b)) are shown. Comparison between Figure 8(a) and Figure 9(a) shows that the initial V_S values are different, probably because of the differences in SWCC and G_0 functions between numerical modelling and field-scale experiment. Nevertheless, the temporal changes of V_S show that V_S decreases during

the water infiltration stages (t = 0—180 min) and increases during the water drainage stages (t = 180—270 min), similar to the observation in the field-scale experiment.

The spatial distribution of the numerically predicted V_S reduction rate (Figure 9(b)) shows a similar trend as that of the field-scale experiment: the V_S reduction starts from the shallow part of the slope (t = 70 and 105 min), and it progresses to a deeper level (t = 180 and 210 min). The result at t = 270 indicates that the drainage of water at the deeper part of the slope does not cause sufficiently the V_S-recovery that is observed in the field-scale measurement (Figure 8(b)). However, we can see that the V_S recovery starts from the deep part of the slope (see contour plots in the result at t = 270 min, Figure 9(b)). Here, we notice that the homogeneous embankment model that we consider, and which consists of a single body of silty sand, does not show the V_S-recovery boundary running parallel to the slope (white dashed line in Figure 8(b) at t = 270 min). However, the permeability distribution can play a major role in determining the spatial distribution of the V_S reduction rate. Therefore, we introduce a second layer in the embankment (core of the embankment) whose boundary runs parallel to the slope (Figure 9(c)). We calculate the V_S reduction rate again. Here we assume that the second layer has a larger permeability than the first layer (approximately 100 times larger than the initial value). Introducing the second layer drastically changes the results, especially at the drainage stages (t > 180 min). The result at t = 270 min (Figure 9(c)) shows that the boundary of the V_S recovery appears, and that the part of this boundary runs approximately parallel to the slope (white dashed line in Figure 9(c)), which is similar to the observation in the field-scale experiment. This finding indicates the presence of heterogeneity in the test embankment.

Finally, we investigate the need of the inclusion of the suction effect in explaining the V_S changes. Our results in Figure 9(b) shows that the maximum V_S reduction rate at Y'=-1.5 m is about 10 %, which is close to that obtained in the field-scale experiment (15%). When we ignore the effect of the suction changes in calculating V_S, i.e., assuming $V_S = \sqrt{G_0^i/\rho(S_r)}$ where G_0^i is the small-strain shear modulus at the initial condition, the result shows that the maximum V_S reduction rate at the same location is about 6 %. This suggests that the density change due to water infiltration does not explain sufficiently the observed magnitude of the V_S reduction, and that it is necessary to consider unsaturated soil properties, i.e., the effect of the suction. This observation corresponds very well to the discussion provided in the previous section.

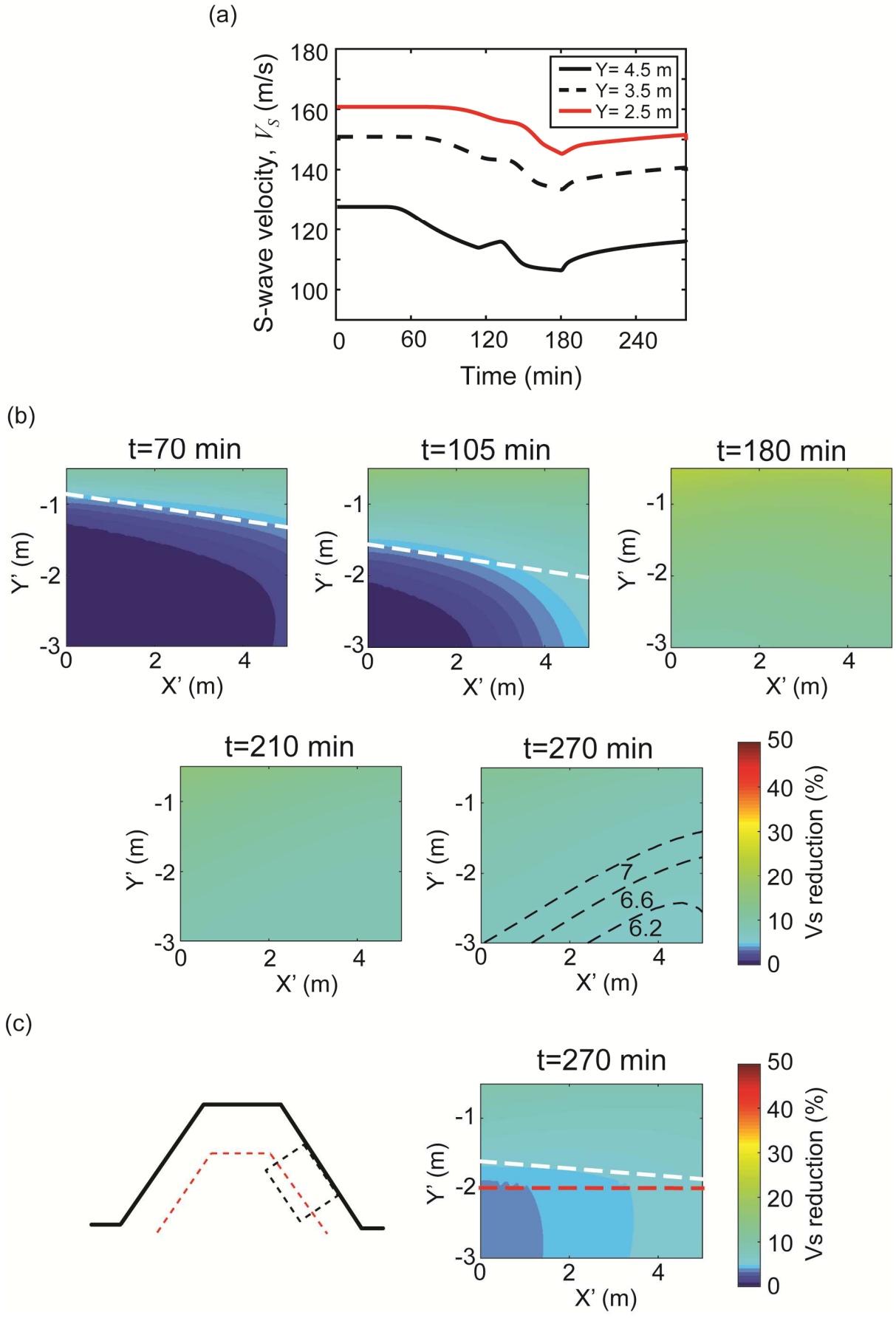

Figure 9: (a) Numerically predicted temporal changes of V_S at three spatial locations shown in Figure 6(a). (b) Numerically predicted spatial distribution of V_S reduction rate R (equation 7). White dashed lines show the spatial boundary corresponding to sharp changes in R. (c) The heterogeneous model containing a core of the embankment and the calculated V_S reduction rate at t = 270 min. The position of the

boundary between the layers is marked by red dashed line. Note the difference from the homogeneous model (t = 270 min in (b)) and the similarity with the results obtained in field-scale experiments (t = 270 min in Figure 8(b)).

6. Conclusion

The unsaturated soil properties, e.g., suction and degree of saturation have a significant influence on the V_S changes due to water infiltration and drainage at an embankment. In order to correctly interpret the measured spatial and temporal V_S changes, a multidisciplinary integrated knowledge of the unsaturated soil is necessary.

We numerically model V_S changes, simultaneously considering fluid transportation in unsaturated soil (seepage analysis) and the small-strain shear modulus as a function of suction and confining stress, using realistic parameters of an embankment (dimension of the embankment, SWCC and rainfall). The results of constant precipitation show clear V_S changes due to water infiltration and drainage. The V_S changes are dictated more by suction changes than by density changes. The field-scale experiment at an artificial embankment with controlled rainfall shows clear indication that water infiltration progresses to a deeper level from the surface and drainage is then followed. Our results of numerical modelling suggest the presence of heterogeneity in the embankment.

Monitoring V_S changes in unsaturated soils can potentially be used to estimate fluid distribution and in-situ, dynamic fluid transportation at the vadose zone. This has many important applications, e.g., in controlling pollution at waste disposal sites, in understanding desertification, in assessing water resources and agricultural sustainability, and in estimating the stability of geoengineering structures and natural slopes.

References

Bear J.. [1972] Dynamics of Fluids in Porous Media, Dover.

Bergamo, P., Dashwood B., Uhlemann S., Swift R., Chambers J.E., Gunn D.A. and Donohue S. [2016]. Time-lapse monitoring of climate effects on earthworks using surface waves. Geophysics 81(2), EN1–EN15.

Collins, B. D. and Znidarcic, D. [2004] Stability analyses of rainfall induced landslides, *Journal of Geotechnical and Geoenvironmental Engineering*, **130**(4), 362-372.

Fredlund, D. G. and Xing, A. [1994] Equations for the soil-water characteristic curve, *Canadian Geotechnical Journal*, **31**(4), 521-532.

Fredlund D. G., Rahardjo H. and Fredlund M. D. [2012] Unsaturated soil mechanics in engineering practice, Wiley.

Ghose, R. and Goudswaard, J. [2004] Integrating S-wave seismic reflection data and cone-penetration-test data using a multiangle multiscale approach, Geophysics, **69**(2), 440-459.

Ghose, R. [2010] Estimating in situ horizontal stress in soil using time-lapse Vs measurements, *in* 'Geophysical Development Series No. 15, Advances in Near-surface Seismology and Ground-penetrating Radar', ed. Miller et al., Society of Exploration Geophysicists, American Geophys. Union, Engineering and Environ. Geophys. Soc., 131-152.

Ghose, R. [2012] A microelectromechanical system digital 3C array seismic cone penetrometer, Geophysics, **77**(3), WA99-WA107.

Green, T. R., Taniguchi, M., Kooi, H., Gurdak, J. J., Allen, D. M., Hiscock, K. M., Treidel, H. and Aureli, A. [2011] Beneath the surface of global change: Impacts of climate change on groundwater, *Journal of Hydrology*, **405**(3), 532-560.

Han, Z. and Vanapalli, S. K. [2016] Stiffness and shear strength of unsaturated soils in relation to soil-water characteristic curve, *Géotechnique*, **66**(8), 627-647.

Hardin, B. O. and Blandford, G. E.[(1989) Elasticity of particulate materials, *Journal of Geotechnical Engineering*, **115**(6), 788-805.

Hayashi, K. and Suzuki, H. [2004] CMP cross-correlation analysis of multi-channel surface-wave data, *Exploration Geophysics*, **35**(1), 7-13.

Holden, P. A. and Fierer, N. [2005] Microbial processes in the vadose zone, *Vadose Zone Journal*, **4**(1), 1-21.

Hoyos, L. R., Suescún-Florez, E. A. and Puppala, A. J. [2015] Stiffness of intermediate unsaturated soil from simultaneous suction-controlled resonant column and bender element testing, *Engineering Geology*, **188**, 10-28.

Konishi, C., Ishizawa, T., Danjo, T. and Sakai, N. [2015] S-wave velocity monitoring during an artificial rainfall experiment using large scale rainfall simulator, *in* 'Near Surface Geoscience 2015, 21st European Meeting of Environmental and Engineering Geophysics'.

Lam, L., Fredlund, D. and Barbour, S. [1987] Transient seepage model for saturated–unsaturated soil systems: a geotechnical engineering approach, *Canadian Geotechnical Journal*, **24**(4), 565-580.

Leong, E. C. and Rahardjo, H. [1997] Permeability functions for unsaturated soils, *Journal of Geotechnical and Geoenvironmental Engineering*, **123**(12), 1118-1126.

Mercer, J. W. and Cohen, R. M. [1990] A review of immiscible fluids in the subsurface: properties, models, characterization and remediation, *Journal of Contaminant Hydrology*, **6**(2), 107-163.

Nuth, M. and Laloui, L. [2008] Effective stress concept in unsaturated soils: Clarification and validation of a unified framework, *International Journal for Numerical and Analytical Methods in Geomechanics*, **32**, 771-801.

Pasquet, S., Bodet, L., Bergamo, P., Guérin, R., Martin, R., Mourgues, R. and Tournat, V. [2016] Small-Scale Seismic Monitoring of Varying Water Levels in Granular Media, *Vadose Zone Journal*, **15**(7).

Park, C., Miller, R. and Xia, J. [1999] Multichannel analysis of surface waves, *Geophysics*, **64**(3), 800-808.

Rahardjo, H., Li, X., Toll, D. G. and Leong, E. C. [2001] The effect of antecedent rainfall on slope stability, Unsaturated Soil Concepts and Their Application in Geotechnical Practice, Springer, 371-399.

Richards, L. A. [1931] Capillary conduction of liquids through porous mediums, *Physics*, **1**(5), 318-333.

Rico, M., Benito, G., Salgueiro, A., Diez-Herrero, A. and Pereira, H. [2008] Reported tailings dam failures: a review of the European incidents in the worldwide context, *Journal of Hazardous Materials*, **152**(2), 846-852.

Sawangsuriya, A., Edil, T. B. and Bosscher, P. J. [2009] Modulus-suction-moisture relationship for compacted soils in postcompaction state, *Journal of Geotechnical and Geoenvironmental Engineering*, **135**(10), 1390-1403.

Scanlon, B. R., Keese, K., Reedy, R. C., Simunek, J. and Andraski, B. J. [2003] Variations in flow and transport in thick desert vadose zones in response to paleoclimatic forcing (0–90 kyr): Field measurements, modeling, and uncertainties, *Water Resources Research*, **39**(7).

Shen, J., Crane, J. M., Lorenzo, J. M. and White, C. D. [2016] Seismic Velocity Prediction in Shallow (< 30 m) Partially Saturated, Unconsolidated Sediments Using Effective Medium Theory, *Journal of Environmental and Engineering Geophysics*, **21**(2), 67-78.

Steenpass, C., Vanderborght, J., Herbst, M., Šimůnek, J. and Vereechen, H. [2010]. Estimating Soil Hydraulic Properties from Infrared Measurements of Soil Surface Temperatures and TDR Data. VADOSE ZONE JOURNAL, 9(4), 910-924.

Takakura, S., Yoshioka, M., Ishizawa, T., and Sakai, N. [2013] Geoelectrical monitoring of the slope of an embankment using a large-scale rainfall simulator, *Proceedings of the 11th SEGJ International Symposium*.

Van Genuchten, M. T. [1980] A closed-form equation for predicting the hydraulic conductivity of unsaturated soils, *Soil Science Society of America Journal*, **44**(5), 892-898.

Yoshioka, M., Takakura, S., Ishizawa, T., and Sakai, N. [2015] Temporal changes of soil temperature with soil water content in an embankment slope during controlled artificial rainfall experiments. *Journal of Applied Geophysics*, **114**, 134–145

Zyserman, F., Monachesi, L. and Jouniaux, L. [2017] Dependence of shear wave seismoelectrics on soil textures: a numerical study in the vadose zone, *Geophysical Journal International*, **208**(2), 918.

List of figure captions

Figure 1: The soil-water characteristic curve (SWCC). Red dots show the experimental data for silty sand (Hoyos et al., 2015). Solid line is the best-fit curve using the model of van Genuchten (1980). Dotted and dashed lines represent curve for sandy soil and clayey soil, respectively.

Figure 2: (a, b) The relationship between the small-strain shear modulus and the suction at different confining stress values: coloured dots/circles show the experimental data (Hoyos et al., 2015) and the continuous lines represent our best-fit estimates (equation 3). (c) The small-strain shear modulus interpolated using equation (3). This surface plot enables us to see G_0 as a continuous function of both variables (suction and confining stress), which is not possible from (a) or (b). Black dots show the experimental data (Hoyos et al., 2015).

Figure 3: (a) Embankment model used in numerical modelling. Small open circles are the spatial locations where the temporal change of elastic properties are calculated and shown in Figure 5. (b) The time series of precipitation used in the numerical modelling. Open circles at the lower margin show times when the spatial distribution of the unsaturated soil properties are investigated (Figure 4), corresponding to the field-scale experiments of Konishi et al. (2015).

Figure 4 (a) Spatial distribution of the estimated suction at each lapse time. t = 0, 70, 105 and 180 min are in water infiltration stage, and t = 210 and 270 min are in water drainage stage (see open circles in Figure 3(b)). (b) Same as (a) but for the degree of saturation. (c) Same as (a) but for the total head. Contour lines and fluid flow vectors (gradient of the total head) are shown in (c).

Figure 5: Temporal change of (a) ρ, (b) G_0 and (c) V_S at three locations shown in Figure 3(a). The vertical dashed line marks the time when the rain stops (t = 180).

Figure 6: (a) Cross-section of the field-scale test embankment and the location of the fixed geophone array. Small open circle are the locations where the temporal changes are monitored (from time-lapse surface wave dispersion data) and shown in Figure 8(a). Dashed rectangle shows the spatial range of the V_s distribution shown in Figure 8(b). (b) The time series of rainfall in this field-scale measurement. Seismic surface wave measurements are made at the time shown by open circles in (b).

Figure 7: (a) Representative waveforms (shot gather) of 1st, 4th, and 6th measurements, when the source is located at the top of the embankment. (b) Dispersion images (MASW) using the data (shot gather) shown in (a). (c) Typical time-lapse dispersion curves picked for all 6 measurements, derived from a shot gather - in this case the source being located at the toe of the embankment (modified after Konishi et al., 2015).

Figure 8: (a) Observed temporal changes of V_S in the field-scale experiment (modified after Konishi et al., 2015). Values at three spatial locations (small open circles in Figure 6(a)) are shown. (b) Spatial distribution of the V_S reduction rate R (equation 7) at each measurement (modified after Konishi et al., 2015).

Positive values of R indicate a decrease of V_S from the initial values. White dashed lines mark the position of the boundary representing sharp changes in the V_S reduction rate, which is interpreted as to be indicating water infiltration and drainage.

Figure 9: (a) Numerically predicted temporal changes of V_S at three spatial locations shown in Figure 6(a). (b) Numerically predicted spatial distribution of V_S reduction rate R (equation 7). White dashed lines show the spatial boundary corresponding to sharp changes in R. (c) The heterogeneous model containing a core of the embankment and the calculated V_S reduction rate at *t* = 270 min. The position of the boundary between the layers is marked by red dashed line. Note the difference from the homogeneous model (*t* = 270 min in (b)) and the similarity with the results obtained in field-scale experiments (*t* = 270 min in Figure 8(b)).